Electronic Supplementary Information

Template-assisted synthesis of hollow anthraquinone-based covalent organic frameworks for aqueous zinc-ion hybrid supercapacitors

Verónica Montes-García,[a] Cataldo Valentini,[b, c] Denys Klymovych,[a] Wojciech Kukułka,[b] Linghao Shi,[a] Violetta Patroniak,[c] Paolo Samorì,*[a] Artur Ciesielski*[a, b]

[a] Université de Strasbourg, CNRS, ISIS 8 allée Gaspard Monge, Strasbourg 67000, France. E-mail: samori@unistra.fr , ciesielski@unistra.fr.

[b] Centre for Advanced Technologies, Adam Mickiewicz University, Uniwersytetu Poznańskiego 10, Poznań 61-614, Poland.

[c] Faculty of Chemistry, Adam Mickiewicz University, Uniwersytetu Poznańskiego 8, Poznań 61-614, Poland.

Table of Contents

Section A. Materials and characterization S2

Section B. Physical characterization S5

Section C. Electrochemical characterization S14

References S19

Section A. Materials and characterization

Materials.1,3,5-triformylphloroglucinol (Tp) (Sigma Aldrich), 2,6-diaminoanthraquinone (DAAQ) (Sigma Aldrich), p-toluenesulfonic acid (PTSA) (Sigma Aldrich), polystyrene (PS) beads 300 nm (Sigma Aldrich), tetrahydrofuran (THF) (Sigma Aldrich), dimethylformamide (DMF) (Sigma Aldrich), zinc foil (thickness of 0.25 mm) (Sigma Aldrich), zinc trifluoromethanesulfonate (Sigma Aldrich), 1-methyl-2-pyrrolidinone (NMP) (Sigma Aldrich), Whatman® qualitative filter paper (cellulose) (Sigma Aldrich), polyvinylidene difluoride (PVDF) (MTI), conductive carbon black Super P (H30253) (Alfa Aesar), coin cells cases (S4R), carbon AvCarb P75 substrate (FuelCellStore).

Methods. The composition, structure, and texture properties of materials were investigated by **powder X-ray powder diffraction (PXRD)** patterns (Bruker D8 X-ray diffractometer). **Thermogravimetric Analyzer (TGA)** decomposition curves were recorded in the range 25-600 °C operating under nitrogen atmosphere, with a thermal step of 10 °C/min on a Mettler Toledo TGA/SDTA851e system. **X-ray Photoelectron Spectroscopy (XPS)** (Thermo Scientific K-Alpha X-ray photoelectron spectrometer) equipped with an aluminum X-ray source (energy 1.4866 keV) at a vacuum level of 10^{-8}-10^{-9} mbar in the main chamber. The spot size of the X-ray beam was fixed at 400 µm. Infrared spectra were acquired with a **Fourier infrared spectrometer (FT-IR)**-4700 JASCO, equipped with an ATR Diamond attachment, in the mid-IR range of 500−4000 cm^{-1}. The specific surface area was measured using a Micromeritics ASAP 2050 surface area and porosity analyzer. Before the **Brunauer-Emmett-Teller (BET)** measurements, the samples were outgassed for 12 hours at 95 °C. Adsorption isotherms were calculated for nitrogen adsorption at 77 K and pressure up to 1 bar. **Scanning (Transmission) Electron Microscopy (S(T)EM)** images were recorded with a FEI Quanta FEG 250 instrument S3 (FEI corporate, Hillsboro, Oregon, USA). **High-resolution transmission electron microscopy** (HRTEM) was performed on a JEOL 2100 F microscope working at 200 kV, equipped with a Cs probe corrector and a GATAN Tridiem imaging filter. The samples were prepared depositing a drop of dispersion on a formvar/carbon on 400 mesh copper grid.

Synthesis of hollow COF DAAQ-Tp and COF DAAQ-Tp

In a 15 mL centrifuge tube, 3 mL of an aqueous dispersion of PS beads (300 nm diameter), 428.01 mg of PTSA (2.49 mmol), and 96.48 mg of DAAQ (0.413 mmol) were added and mixed completely using a vortex shaker for 10 minutes. Then, 57 mg of Tp (0.27 mmol) was added, and the mixture

was shaken again for approximately 30 minutes until the colour changed from brick-red to orange-yellow. The reaction mixture was poured in a 4 cm petri dish to facilitate the water evaporation and the petri dish was placed heated at 80 °C for 24 hours. The solid was washed with water (3 x 5 mL) and DMF (3 x 5 mL) and further purified by Soxhlet extraction with THF for 16 hours. The product was finally dried in a vacuum oven at 60 °C for 3 hours and 82 mg of hollow COF-DAAQ-Tp were obtained. The synthesis of COF-DAAQ-Tp followed a similar procedure, but instead of using PS beads, 3 mL of water was used.

Fabrication of Zinc hybrid supercapacitors (Zn-HSCs). Zinc foil was directly used as an anode electrode after being polished with gauze and pouched into electrodes with an 8 mm diameter. The cathode electrode is composed of 60 wt% of COF or hollow COF, 30 wt% of super P as conductive agent, and 10 wt% of PVDF as the binder. NMP solvent was added to the above mixture and then the mixture was coated onto carbon paper electrodes. The electrodes were dried in a vacuum oven at 80 °C overnight. Zn-HSCs were assembled with the electrolyte of 4 M $Zn(CF_3SO_3)_2$ aqueous solution, a Whatman® qualitative filter paper (cellulose) as a separator, and a coin 2032 battery shell. For each electrode, the mass loading was 1 mg cm^{-2}.

Electrochemical characterizations and calculations of aqueous Zn-HSCs

The electrochemical performance of Zn-HSCs was studied using cyclic voltammetry (CV), and electrochemical impedance spectroscopy (EIS) on Autolab PGSTAT128N Potentiostat / Galvanostat instruments with a Metrohm Autolab DuoCoin Cell Holder (Metrohm AG) at room temperature. CV was performed at scan rates of 0.01 – 1 V/s in the voltage range between 0 and 1.8 V. EIS measurement was recorded with a frequency range of 0.01 Hz to 1 MHz. The galvanostatic charge-discharge (GCD) tests were carried out on Neware Battery Tester (BTS-4008T-5V/10mA, Neware Technology Company, Guangdong, China). GCD curves were tested at current densities ranging from 0.1 to 1 A/g.

Electrochemical calculations

Calculation of the specific capacitances: The specific capacitance was calculated using GCD with following equation:

$$C_s = \frac{2 \cdot I \cdot \Delta t}{\Delta V \cdot m} \qquad \text{(eq. 1)}$$

Where, I (A) is the response current, Δt (s) is the discharge time, ΔV (V) is the voltage window and m (g) is the mass of COF-DAAQ-Tp or hollow COF-DAAQ-Tp in a single electrode.

Power and energy density calculations

The energy density of the device was obtained from the formula:

$$E = \frac{I}{3.6 \times m} \times \int_0^{\Delta t} V\, dt \qquad \text{(eq. 2)}$$

The power density of the device was calculated from the formula:

$$P = \frac{E}{\Delta t} \cdot 3600 \qquad \text{(eq. 3)}$$

Where, E is specific energy (Wh kg^{-1}), $\int_0^{\Delta t} V\, dt$ (V s) is the integral area of the discharge curve, P is power density (W kg^{-1}).

Calculations for the kinetics of the electrochemical processes occurring at both electrode materials:

$$i = av^b. \qquad \text{(eq. 4)}$$

Where i (A) is the peak current, v (V/s) the scan rate, a and b are variable parameters.

$$i = k_1 v + k_2 v^{1/2} \qquad \text{(eq. 5)}$$

Where $k_1 v$ and $k_2 v^{1/2}$ represent the capacitive and diffusion-limited effects, respectively.

Section B. Physical characterization

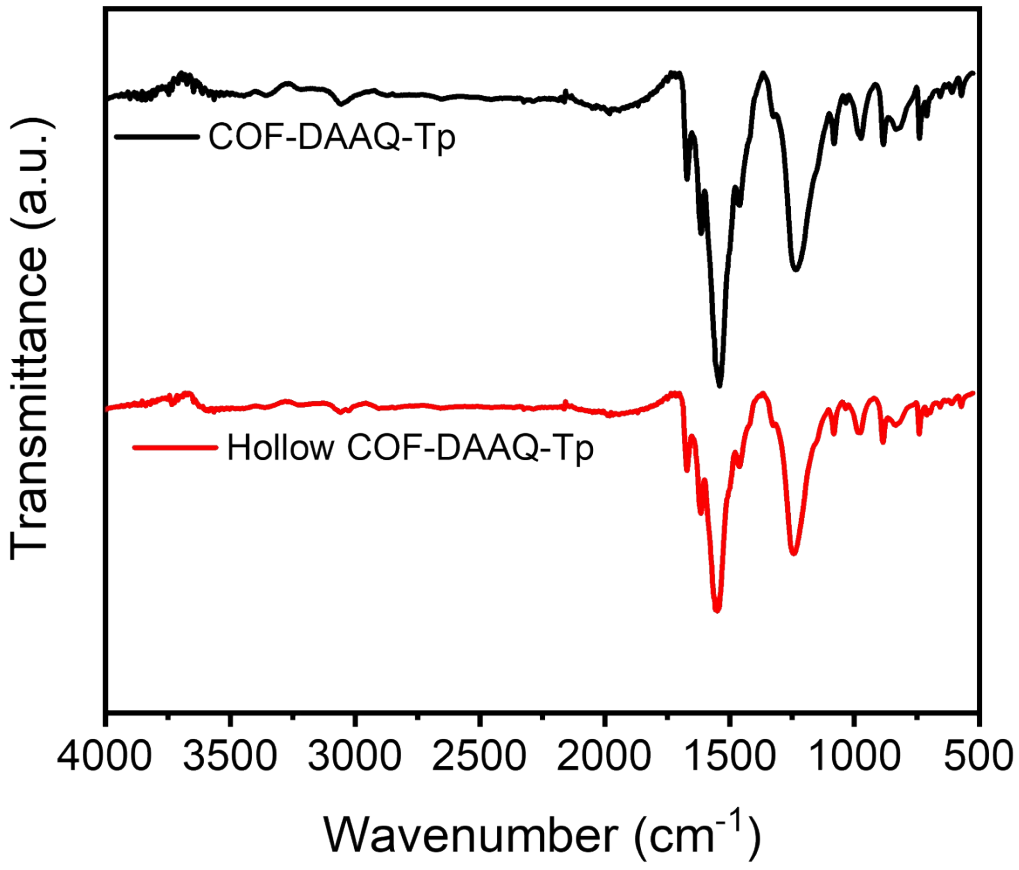

Fig.S1. FTIR spectra of COF-DAAQ-Tp (black curve) and hollow COF-DAAQ-Tp (red curve).

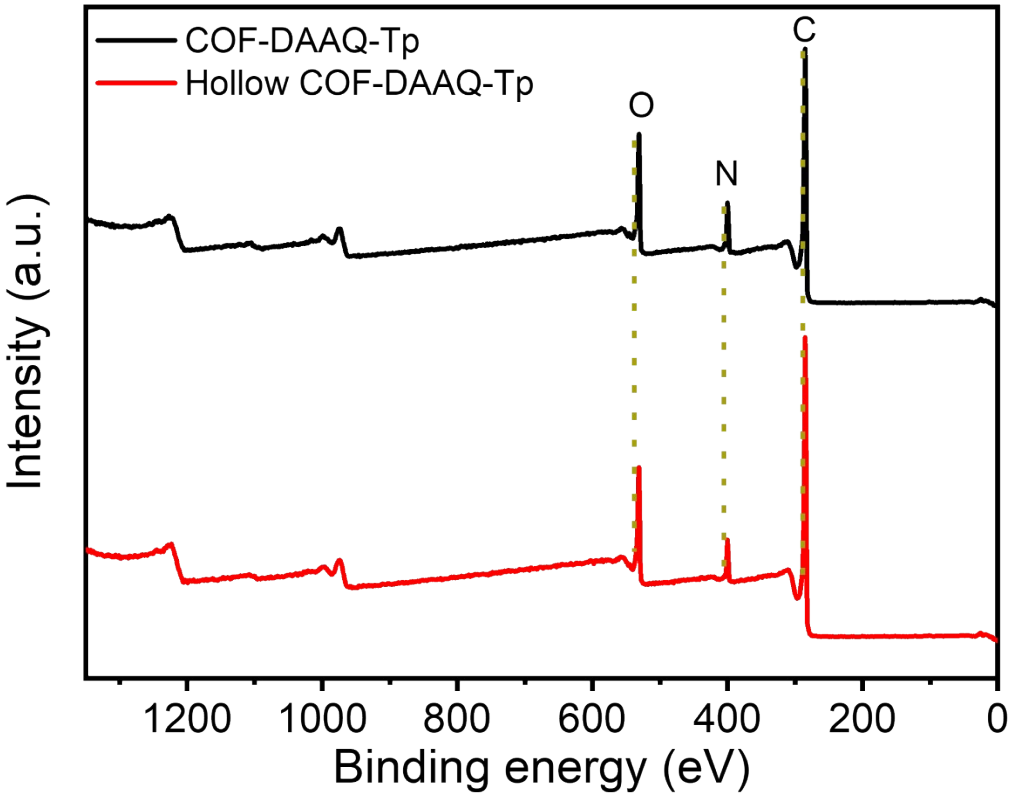

Fig.S2. XPS survey of COF-DAAQ-Tp (black curve) and hollow COF-DAAQ-Tp (red curve).

The XPS survey spectra of COF-DAAQ-Tp (black spectrum) and hollow COF-DAAQ-Tp (red spectrum) show the solely presence of the C, N, and O atoms.

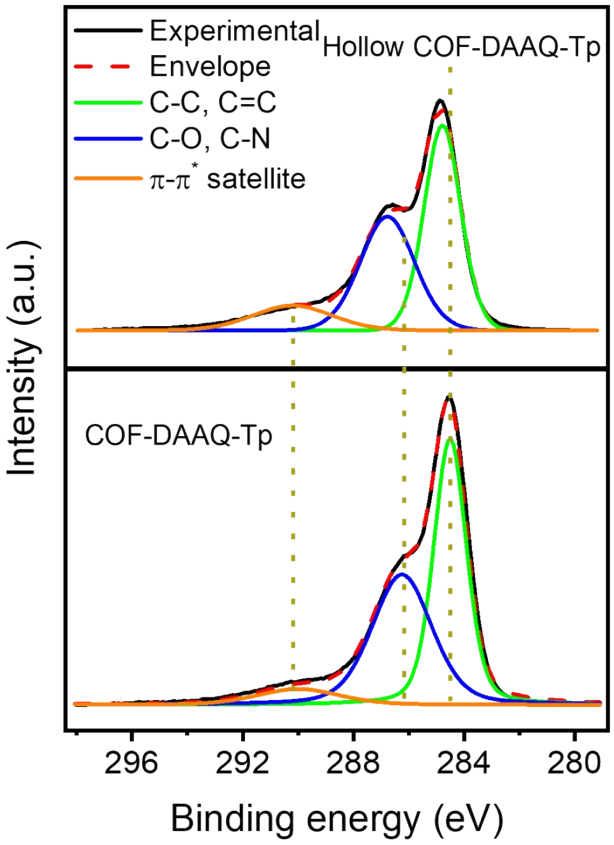

Fig. S3. C1s XPS analysis of the COF-DAAQ-Tp (bottom), and hollow COF-DAAQ-Tp (top).

The high-resolution C1s spectra of COF-DAAQ-Tp and hollow COF-DAAQ-Tp reveal in both cases two main peaks at 284.5 and 286.2, which correspond to the binding energies of carbon-carbon bonds (C-C, C=C) and carbon-heteroatom bonds (C-O, C-N), respectively.

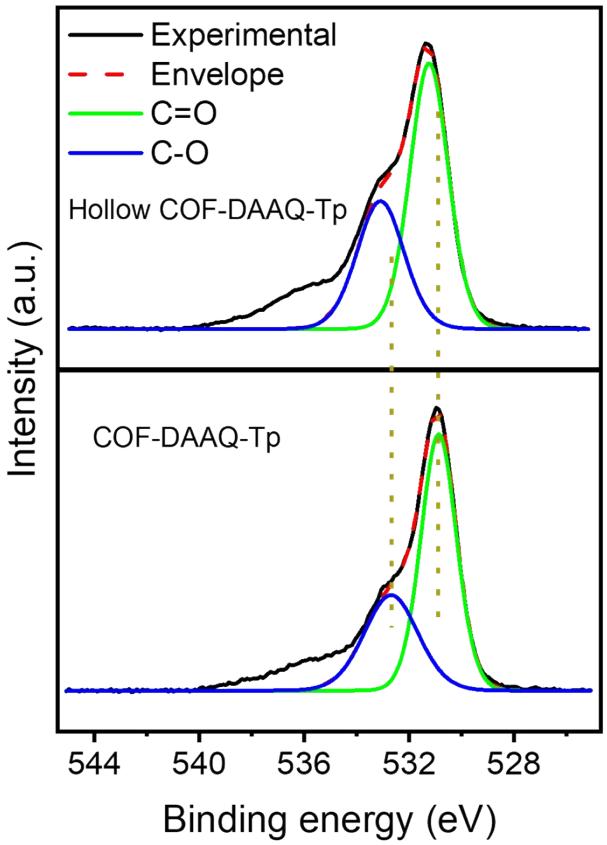

Fig. S4. O1s XPS analysis of the COF-DAAQ-Tp (bottom), and hollow COF-DAAQ-Tp (top).

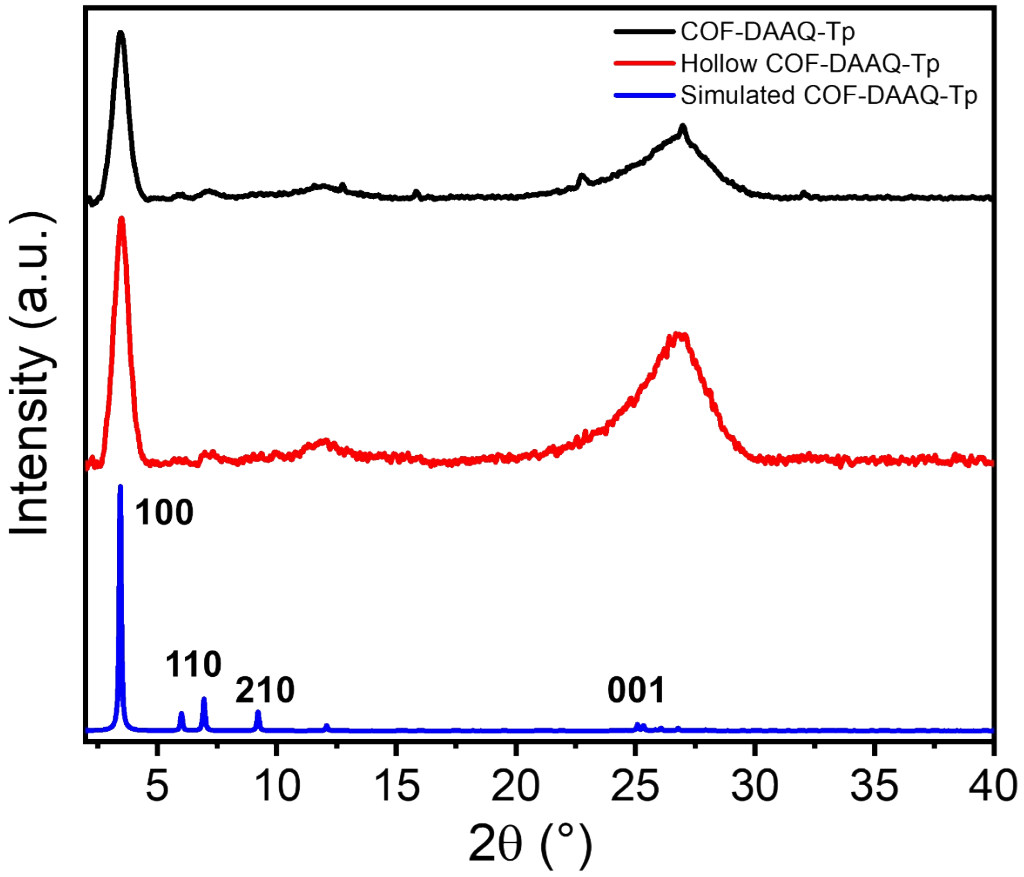

Fig. S5. PXRD patterns of COF-DAAQ-Tp (black curve), and hollow COF-DAAQ-Tp (red curve) and simulated COF-DAAQ-Tp (blue curve).

Sherrer equation:
$$D = \frac{K\lambda}{\beta \cos\theta} \qquad \text{(eq. 6)}$$

where D (nm) – mean size of the crystalline domains, K – shape factor, λ (nm) – X-ray wavelength, β (rad.) - line broadening at half the maximum intensity, θ (°) – Bragg angle.

The size of crystalline domains was calculated from the Scherrer equation (eq. 6), and it amounts to 10.44 and 10.81 nm for COF-DAAQ-Tp and hollow COF-DAAQ-Tp, respectively.

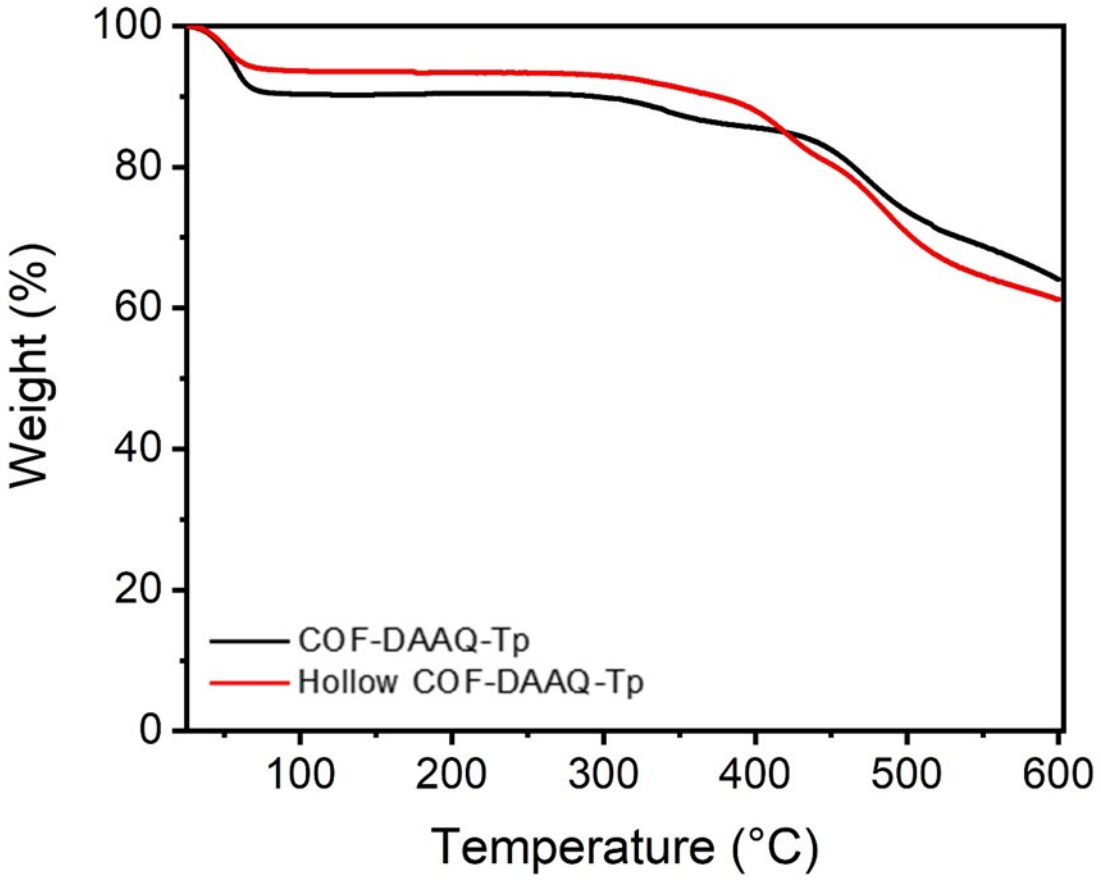

Fig. S6. TGA results of COF-DAAQ-Tp (black curve) and hollow COF-DAAQ-Tp (red curve).

The 10 % weight loss observed below 100 ºC likely corresponds to the loss of adsorbed or residual water molecules. This is a common occurrence for materials synthesized in aqueous environments, where water can be physically adsorbed onto the surface or trapped within the pores of the material. The weight loss at such low temperatures indicates the evaporation of these weakly bound water molecules.

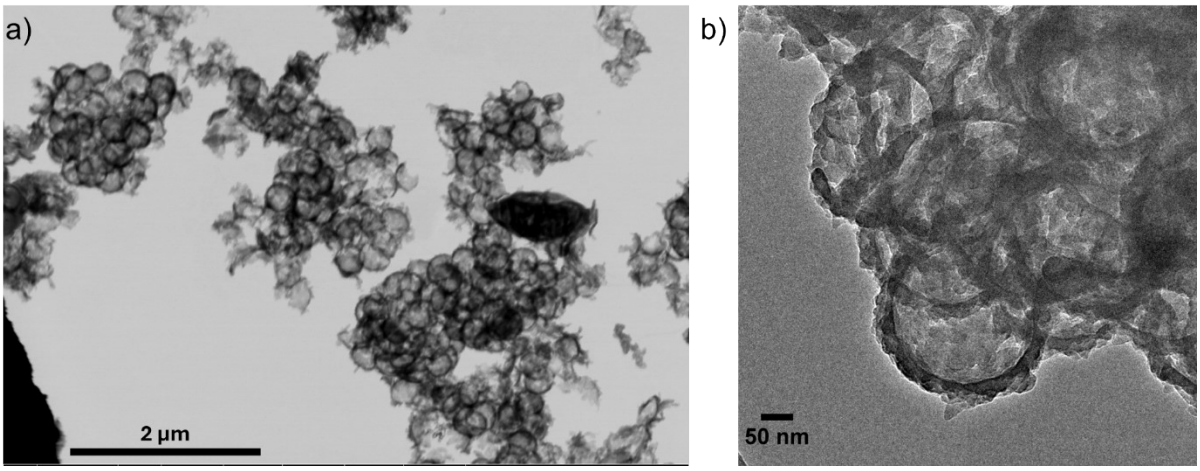

Fig. S7. a) STEM image and b) HRTEM image of hollow COF-DAAQ-Tp.

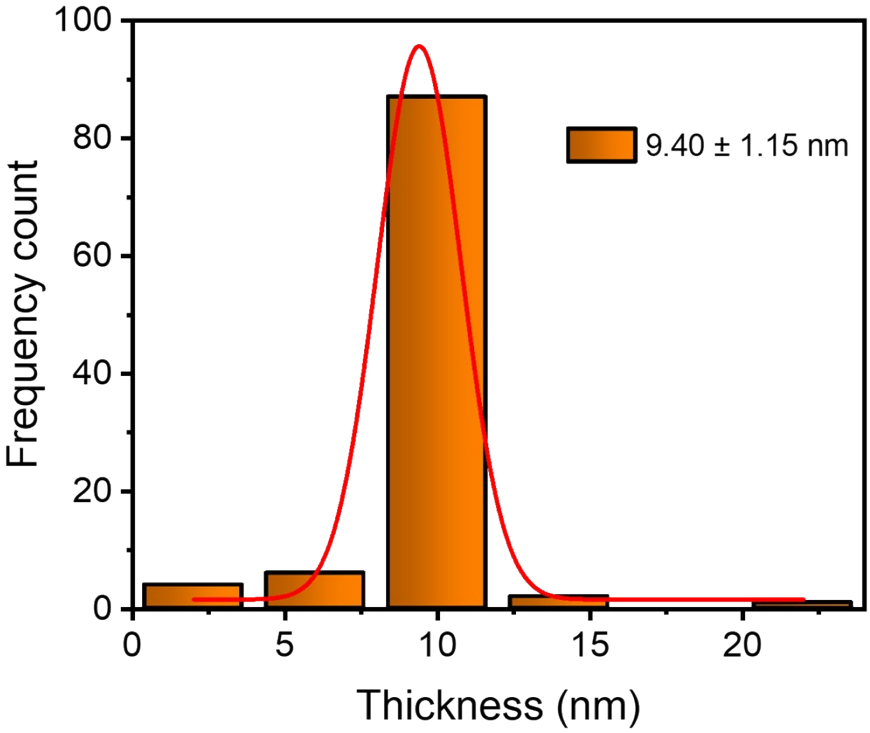

Fig. S8. Average thickness of the COF shell calculated from the SEM images of PS@COF-DAAQ-Tp.

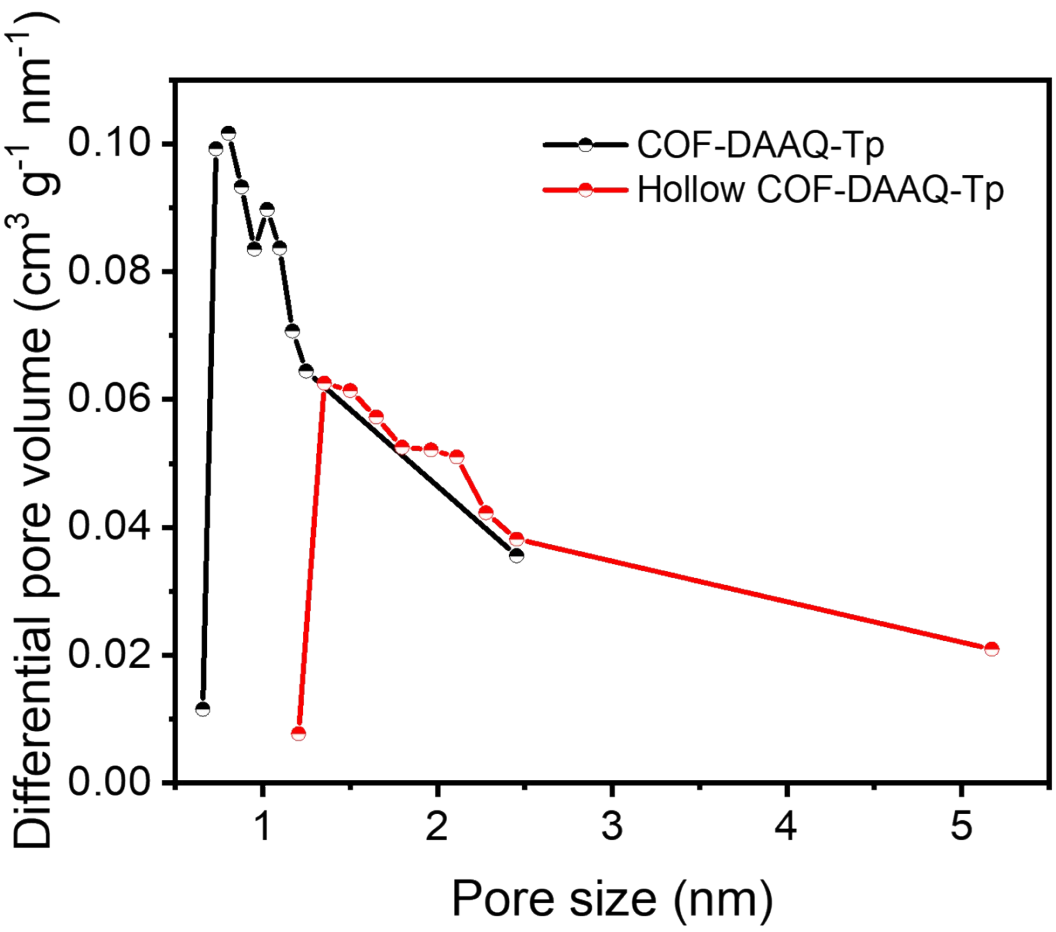

Fig. S9. Pore size distribution of COF-DAAQ-Tp (black curve) and hollow COF-DAAQ-Tp (red curve).

Section C. Electrochemical characterization

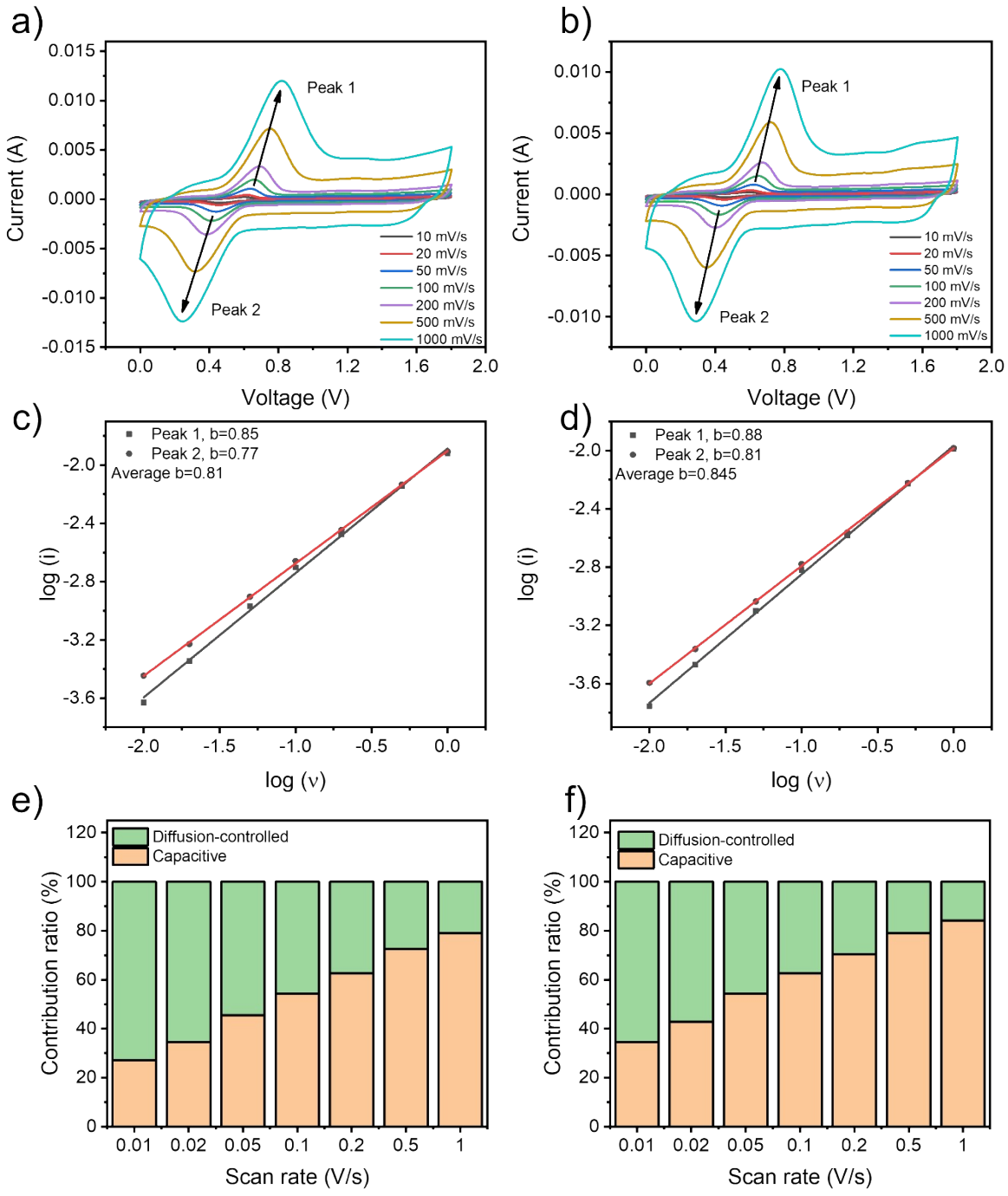

Fig. S10. a-b) CV curves at different scan rates (0.01 – 1 V/s), c-d) linear fit of log(i) versus log(v) for evaluation *b* parameter, e-f) capacitive and diffusion-controlled contribution at different scan rates (0.01 – 1 V/s) of a, c, e) COF-DAAQ-Tp and b, d, f) hollow COF-DAAQ-Tp.

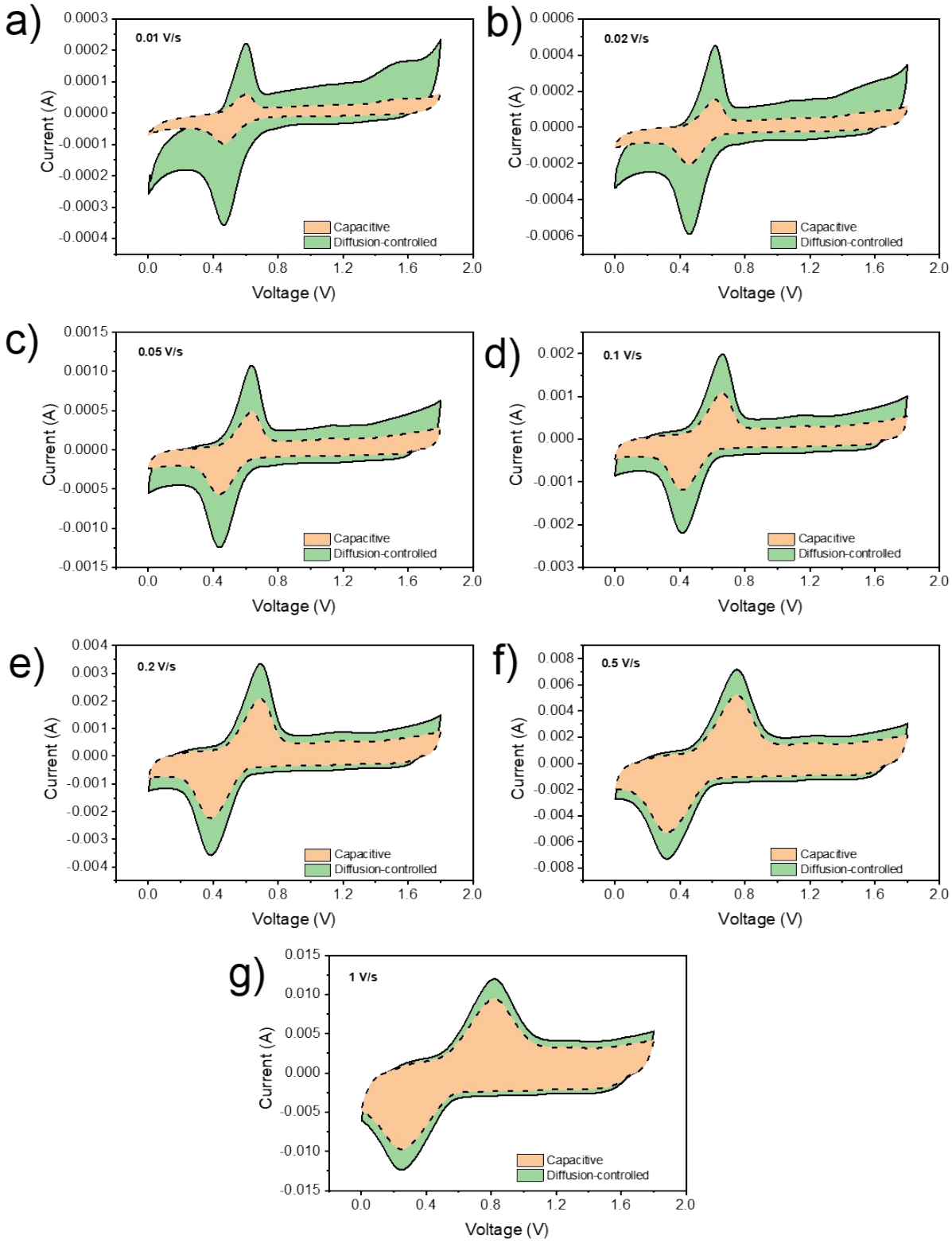

Fig. S11. Capacitive and diffusion-controlled contribution fraction for COF-DAAQ-Tp at different scan rates (0.01 – 1 V/s).

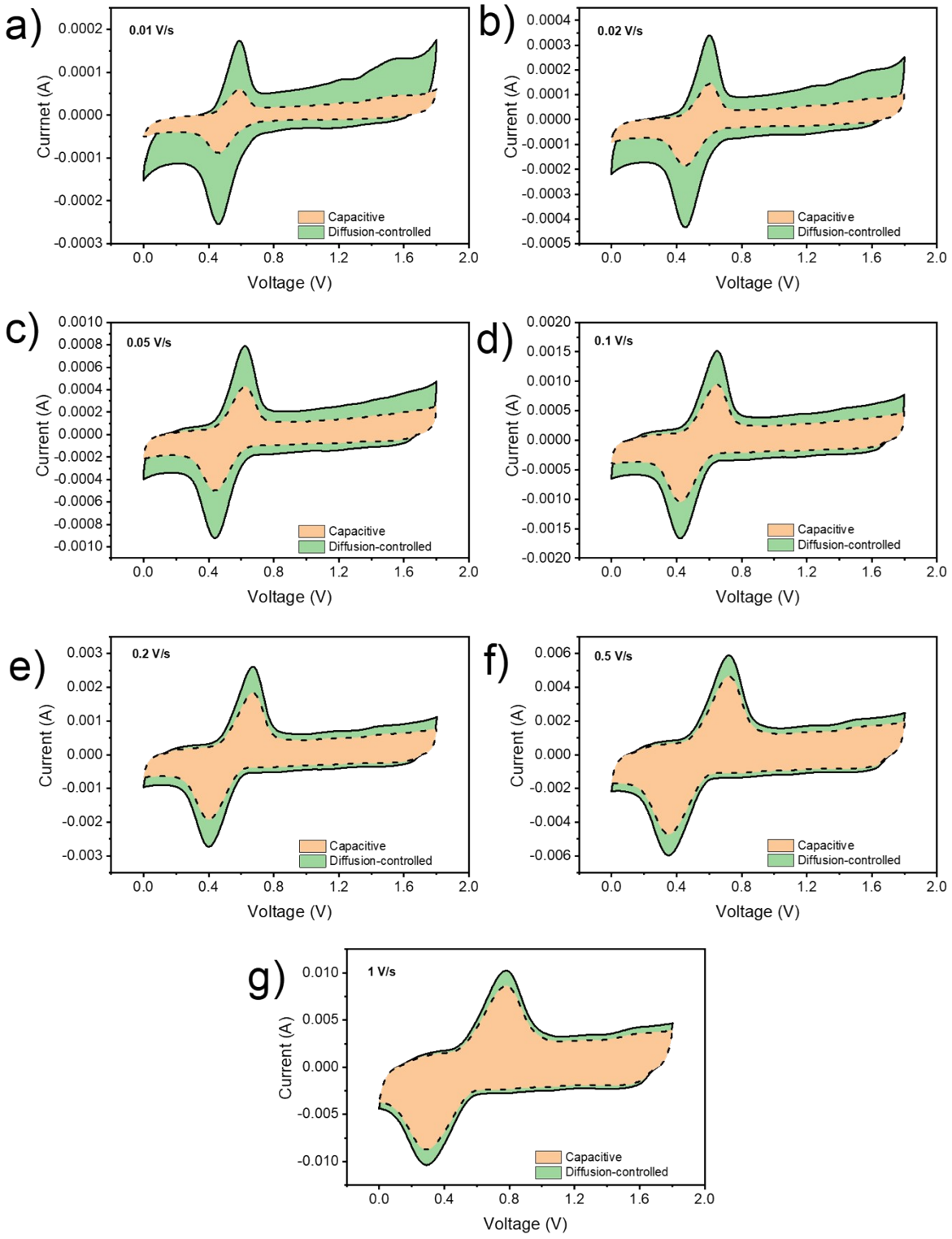

Fig. S12. Capacitive and diffusion-controlled contribution fraction for hollow COF-DAAQ-Tp at different scan rates (0.01 – 1 V/s).

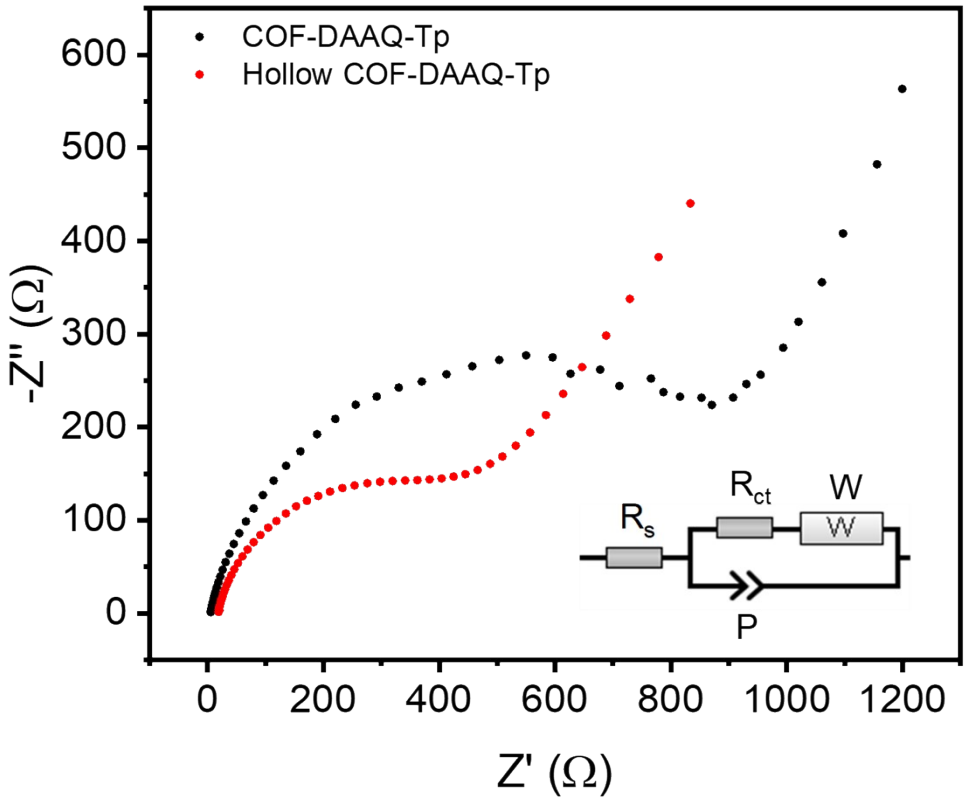

Fig. S13. Nyquist plot for COF-DAAQ-Tp (black dots) and hollow COF-DAAQ-Tp (red dots) with equivalent electric circuit model where R_s – the intrinsic resistance, R_{ct} – the charge transfer resistance, W – Warburg element (represents diffusion in the system), P – constant phase element (represents the EDLC part of the device).

Table S1. State of the art of the electrochemical performance of various cathode materials in Zn-HSCs.

Cathode	Anode	Electrolyte	Voltage window (V)	Capacitance/ Capacity	Cyclability	Energy density (Wh/kg)	Power density (kW/kg)	Surface area (m^2/g)	Ref.
Hollow COF-DAAQ-Tp	Zn foil	4 M $Zn(CF_3SO_3)_2$	0-1.8	142.1 F/g (0.1 A/g)	70% (5000 cycles)	17.8	0.604	344	This work
COF-DAAQ-Tp	Zn foil	4 M $Zn(CF_3SO_3)_2$	0-1.8	75.4 F/g (0.1 A/g)	53% (5000 cycles)	8.67	0.698	257	This work
PCNs	Zn foil	1 M $ZnSO_4$	0.1-1.7	149 mAh/g (0.2 A/g)	91% (10000 cycles)	60	15.976	2671.9	[1]
$RuO_2 \cdot H_2O$	Zn foil	2 M $Zn(CF_3SO_3)_2$	0.4-1.6	122 mAh/g (0.1 A/g)	87.5 (10000 cycles)	82	16.74	-	[2]
AC	2D-Zn/Ni	1 M $ZnSO_4$	0.2-1.8	468 F/g (0.5 A/g)	99% (10000 cycles)	208	20	2201	[3]
rGO-MXene	Zn foil	2 M $ZnSO_4$	0.2-1.6	129 F/g (0.4 A/g)	95% (75000 cycles)	35	4	-	[4]
MnO_2@CAC	Zn foil	2 M $ZnSO_4$ + 0.1 M $MnSO_4$	0.8-1.9	281.6 mAh/g (0.36 A/g)	80.7 % (16000 cycles)	90	0.239	-	[5]
PC	Zn foil	3 M $Zn(CF_3SO_3)_2$	0-1.8	326 F/g (0.5 A/g)	96.7% (10000 cycles)	130.1	0.18	2125	[6]
PA-COF	Zn foil	1 M $ZnSO_4$	0.2-1.6	247 mAh/g (0.1 A/g)	99.64 % (10000 cycles)	-	-	19.6	[7]
PC induced by $ZnCl_2$	Zn foil	2 M $ZnSO_4$	0.2-1.8	120.3 mAh/g (0.5 A/g)	99.2% (10000 cycles)	103.2	-	1801.6	[8]
HAQ-COF	Zn foil	2 M $ZnSO_4$	0.2-1.8	339 mAh/g (0.1 A/g)	85 % (10000 cycles)	75	3.262	53	[9]
N and O co-doped C	Zn foil	2 M $ZnSO_4$	0.2-1.8	138.5 mAh/g (0.5 A/g)	100% (10000 cycles)	110	20	197.45	[10]
Graphene@PANI	Zn foil	2 M $ZnSO_4$	0.4-1.6	154 mAh/g (0.1 A/g)	80.5% (6000 cycles)	138	2.45	-	[11]
N and Ov enriched $NiCo_2O_4$@CC	Zn foil	6 M KOH + 0.2 M $Zn(CH_3COO)_2$	0-0.5	825.2 F/g (1 A/g)	98% (5000 cycles)	50.3	0.3	36.71	[12]

PCN – porous carbon nanosheet, AC – activated carbon, rGO – reduced graphene oxide, CAC, CC – carbon cloth, PC – porous carbon, Ov – oxygen vacancies

References

[1] D. Wang, Z. Pan, Z. Lu, *Micropor. Mesopor. Mat.* **2020**, 306, 110445.

[2] L. Dong, W. Yang, W. Yang, C. Wang, Y. Li, C. Xu, S. Wan, F. He, F. Kang, G. Wang, *Nanomicro Lett.* **2019**, 11, 94.

[3] G.-H. An, J. Hong, S. Pak, Y. Cho, S. Lee, B. Hou, S. Cha, *Adv. Energy Mater.* **2020**, 10, 1902981.

[4] Q. Wang, S. Wang, X. Guo, L. Ruan, N. Wei, Y. Ma, J. Li, M. Wang, W. Li, W. Zeng, *Adv. Electron. Mater.* **2019**, 5, 1900537.

[5] J. Shi, S. Wang, Q. Wang, X. Chen, X. Du, M. Wang, Y. Zhao, C. Dong, L. Ruan, W. Zeng, *J. Power Sources* **2020**, 446, 227345.

[6] H. Li, J. Wu, L. Wang, Q. Liao, X. Niu, D. Zhang, K. Wang, *Chem Eng J* **2022**, 428, 131071.

[7] W. Wang, V. S. Kale, Z. Cao, S. Kandambeth, W. Zhang, J. Ming, P. T. Parvatkar, E. Abou-Hamad, O. Shekhah, L. Cavallo, M. Eddaoudi, H. N. Alshareef, *ACS Energy Lett.* **2020**, 5, 2256.

[8] S. Yang, Y. Cui, G. Yang, S. Zhao, J. Wang, D. Zhao, C. Yang, X. Wang, B. Cao, *J. Power Sources* **2023**, 554, 232347.

[9] W. Wang, V. S. Kale, Z. Cao, Y. Lei, S. Kandambeth, G. Zou, Y. Zhu, E. Abouhamad, O. Shekhah, L. Cavallo, M. Eddaoudi, H. N. Alshareef, *Adv. Mater.* **2021**, 33, 2103617.

[10] X. Deng, J. Li, Z. Shan, J. Sha, L. Ma, N. Zhao, *J. Mater. Chem. A* **2020**, 8, 11617.

[11] J. Han, K. Wang, W. Liu, C. Li, X. Sun, X. Zhang, Y. An, S. Yi, Y. Ma, *Nanoscale* **2018**, 10, 13083.

[12] X. Zhang, M. S. Javed, X. Zhang, S. Ali, K. Han, A. Ahmad, I. Hussain, A. M. Tighezza, W. U. Arifeen, W. Han, *J. Energy Storage* **2024**, 86, 111208.